Güemes, A., Sanmiguel Vila, C., Örlü, R., Vinuesa, R., Schlatter, P., Ianiro, A. & Discetti, S. (2019). Flow organization in the wake of a rib in a turbulent boundary layer with pressure gradient. *Experimental Thermal and Fluid Science*, vol. 108, pp. 115–124.

DOI: 10.1016/j.expthermflusci.2019.05.022

Flow organization in the wake of a rib in a turbulent boundary layer with pressure gradient

A. Güemes[a,*], C. Sanmiguel Vila[a], R. Örlü[b], R. Vinuesa[b], P. Schlatter[b], A. Ianiro[a], S. Discetti[a]

[a]*Aerospace Engineering Research Group, Universidad Carlos III de Madrid, Leganés, Spain*
[b]*Linné FLOW Centre, KTH Mechanics, SE-100 44 Stockholm, Sweden*

Abstract

The effect of a streamwise pressure gradient on the wake developed by wall-attached square ribs in a turbulent boundary layer is investigated experimentally. Favourable-, adverse- and zero-pressure-gradient conditions (FPG, APG and ZPG, respectively) are reproduced at matched friction Reynolds number and non-dimensional rib height. Flow-field measurements are carried out by means of Particle Image Velocimetry (PIV). Turbulence statistics are extracted at high resolution using an Ensemble Particle Tracking Velocimetry approach. Modal analysis is performed with Proper Orthogonal Decomposition (POD). We demonstrate that a non-dimensional expression of the pressure gradient and shear stress is needed to quantify the pressure-gradient effects in the wake developing past wall-attached ribs. We suggest the Clauser pressure-gradient parameter β, commonly used in the literature for the characterization of turbulent boundary layers under the effect of a pressure gradient, as a suitable parameter. The results show that, in presence of an adverse pressure gradient, the recirculation region downstream of the rib is increased in size, thus delaying the reattachment, and that the peak of turbulence intensity and the shed eddies are shifted towards larger wall-normal distances than in the ZPG case. The observed changes with respect to the ZPG configuration appear more intense for larger magnitude of β, which are more likely to be obtained in APG than in FPG due to the reduced skin friction and increased displacement thickness.

Keywords: Turbulent boundary layer, Pressure gradient flows, Ribs

1. Introduction

Wall-attached ribs are used in a diverse portfolio of industrial applications (e.g. turbomachinery and electronic hardware) as an effective passive strategy of enhancing the convective heat transfer (see, e.g., Refs. [1, 2]). The appeal and the simplicity of such passive devices triggered a wide scientific interest [3, 4, 5, 6, 7] which continues unabated [8, 9].

Due to its practical relevance, simplified scenarios such as the inclusion of ribs in zero pressure gradient (ZPG) turbulent boundary layers (TBLs) developing over a flat plate or in channel flows have widely been explored over the years in order to understand the effects of the geometry of the ribs on the flow-field features and heat-transfer characteristics. For instance, Han et al. [4] investigated the effects of rib shape, angle and pitch-to-height ratio in channel flows, showing that 45° ribs produce higher Nusselt number (Nu) values than 90° ribs with the same overall friction drag. For the case of ZPG TBLs, an extensive study of the turbulent statistics downstream of wall-mounted ribs was carried out by Castro and Epik [10]. In their work, it was reported that the development process of a boundary layer after a rib is not significantly affected by the outer boundary conditions, i.e. the change in free-stream turbulence. Moreover, they compared their results with other works with separated flows past ribs with different geometries, showing that the geometry did not affect the development of the boundary layer. Evidences are also provided on the minor role played by free-stream turbulence in this process. A similar effect has been observed by Hearst et al. [11] for wall-mounted cubes in ZPG TBLs. The flow downstream of the rib is mainly dominated by eddies shed by the rib [8, 9] which superpose on the large-scale motions dominating the outer region of TBLs. The effect of these vortical structures on the heat-transfer efficiency was recently studied by Mallor et al. [9]. In their study, flow-field and heat-transfer measurements downstream of wall-proximity ribs were combined to explore the correlation between instantaneous flow-field and wall convective heat-transfer features. Their results provide a statistical evidence of a direct relation between the coherence of near-wall flow features and heat-transfer enhancement.

Despite these advances, most flows of relevance in technical applications are exposed to pressure gradients in which the applicability of the knowledge from ZPG TBL flows is restricted. In particular, it has been shown that turbulent boundary layers with adverse pressure gradients (APG) present Stanton number values analogous to ZPG TBLs [12], but with significantly lower skin-friction coefficient than in ZPG flows [12, 13]. Although this makes APG TBLs an outstanding candidate for the design of high-performance heat exchangers, the flow downstream of wall-mounted ribs immersed in TBLs developing under the effect of a pressure gradient is a much less explored topic. The majority of the older studies available analyzes the case of backward facing steps. Kuehn [14] analyzed the effect of the adverse pressure gradient on the reattachment length in a parallel-walled channel with a backward facing step. The results highlight that the reattachment length for fully-developed

*Corresponding author
Email address: sdiscett@ing.uc3m.es (S. Discetti)

Nomenclature

β	Clauser pressure-gradient parameter
δ^*	displacement thickness
δ_{99}	boundary-layer thickness
$\overline{x_r}$	mean reattatchment point
$\overline{y_0}$	mean stagnation point
τ_w	mean wall-shear stress
θ	momentum thickness
$\underline{\underline{\Lambda}}$	singular value matrix
$\underline{\underline{\Phi}}$	spatial basis
$\underline{\underline{\Psi}}$	temporal basis
H_{12}	shape factor
k	rib side length
Nu	Nusselt number
Re_{δ^*}	displacement thickness Reynolds number
Re_τ	friction Reynolds number
Re_θ	momentum thickness Reynolds number
St	Strouhal number
U_∞	free-stream velocity
u_τ	wall friction velocity
$\mathrm{d}P/\mathrm{d}x$	pressure gradient along the streamwise direction
APG	adverse pressure gradient
EPTV	ensemble particle tracking velocimetry
FPG	favourable pressure gradient
PIV	particle image velocimetry
POD	proper orthogonal decomposition
RANS	Reynolds-averaged Navier–Stokes
SST	shear stress transport
TBL	turbulent boundary layer
ZPG	zero pressure gradient

turbulent flow in parallel-walled channels depends mainly on the adverse pressure gradient created due to the presence of the backward facing step, while the effect of the inflow conditions is of minor importance. The reattachment length was observed to increase with the intensity of the adverse pressure gradient. Pressure-gradient effects on the reattachment length were further studied by Ra and Chang [15]. In their results, Ra and Chang [15] also concluded that the reattachment length under the effect of a non-constant increasing streamwise adverse pressure gradient was larger than its constant counterpart. In the two previously mentioned studies the flow is characterized only in terms of reattachment length after separation, but not in terms of turbulence statistics. Neither of the two previous studies reported profiles of the mean velocity or turbulence statistics in the separated and/or reattachment regions of a parallel-walled channel with a backward facing step. A statistical characterization of the backward facing step flow is reported by Driver and Seegmiller [16]. Their results show that the momentum and the displacement thickness increase with the pressure gradient. Furthermore, they showed that the shape and growth of the Reynolds stresses was independent of the intensity of the pressure gradient.

Regarding the effect of a pressure gradient in a channel flow with turbulent square ribs, recent experimental studies have been reported in Refs. [17, 18, 19]. They showed that, unlike in canonical near-wall turbulent flows, the convective and diffusion terms in the turbulent kinetic energy transport equation were not negligible in the separated region of the flow. Furthermore, Ref. [19] also reports the modal analysis for the same database, showing a reduction of energy in the first modes due to the destruction of large-scale motions when compared with canonical turbulent channel flows without ribs; this result is in agreement with the recent findings reported in Refs. [8, 9]. Shah and Tachie [17] report that the APG affects the flow statistics across a larger portion of the channel when compared with the flow under favourable pressure gradient (FPG). This can be explained in terms of pressure-gradient effects on the boundary layer thickness.

Unfortunately, most of these studies suffer a lack of characterization of the inflow turbulent statistics and, above all, of the pressure gradient parameters, which substantially hinders the generalization of the results. It is well known that the investigation of APG TBLs involves a larger parametric space than ZPG, which includes not only the local pressure gradient but also its upstream (pressure-gradient) history in the evolution of the TBL. Furthermore, there is no agreement about the non-dimensional parameters that should be used in order to characterize the pressure-gradient effect [24**?**]. Despite this, the most commonly parameter used to determine the pressure-gradient strength is the Clauser pressure-gradient parameter, β. Clauser [20] proposed the parameter $\beta = \delta^*/\tau_w \mathrm{d}P/\mathrm{d}x$ where δ^* is the displacement thickness, τ_w is the mean wall-shear stress, and $\mathrm{d}P/\mathrm{d}x$ the pressure gradient along the streamwise direction; β quantifies the relative importance of the forces due to the lo-

cal pressure gradient and shear stress. Regrettably, the inclusion of β results in a wider parametric space with respect to ZPG TBLs. In an attempt to reduce the number of parameters which characterize APG flows, most of the APG studies are performed in a state of near-equilibrium. According to Townsend [21], TBLs reach near-equilibrium conditions if the free-stream velocity follows a power-law relation. One possible option to reach this condition is the establishment of a constant β along the evolution of the TBL. However obtaining constant-β conditions is extremely challenging [22]. Vinuesa et al. [13] have shown that, when analyzing flows with non-constant β, the upstream β-history can be expressed in terms of an *accumulated* β.

In this framework, it is of the deepest relevance to determine if β is a useful parameter for the analysis of APG TBLs flows with ribs. Assuming this is the case, it is quite interesting to assess how the pressure gradient affects the wake downstream of the rib and the flow structures present in the flow. This knowledge would allow to determine whether streamwise pressure gradients could be used to control the flow-field features in TBLs with wall-attached ribs.

In the present work, we investigate the effects of different pressure gradients (favourable and adverse) on the flow development past wall-attached ribs in TBLs. With this purpose, experiments are performed on a TBL developing on a flat plate in a subsonic wind tunnel. The β parameter is characterized for FPG, ZPG and APG. Experiments are performed at constant friction Reynolds number Re_τ, which has been shown to be a suitable quantity for the analysis of moderate β TBLs for a fixed scale separation [23, 24]. The rib heights k are chosen to have in all the experiments the same ratio k/δ_{99}, with the aim of isolating the effect of the pressure gradient. To the best of the authors knowledge, such analysis is lacking in the literature. Particle Image Velocimetry (PIV) is used to extract flow fields for subsequent modal analysis with Proper Orthogonal Decomposition (POD). Turbulent statistics are obtained at higher resolution than PIV using an Ensemble Particle Tracking Velocimetry approach, thus obtaining a combination of a large field of view and high level of detail in the statistics.

The paper is structured as follows: Section 2 reports a description of the experimental setup, together with the strategies used to post-process the acquired data. The turbulence statistics at several positions downstream of the rib are presented in Section 3, along with the mean flow-field distributions to identify the features of each configuration. The modal analysis of the instantaneous flow-fields is presented in Section 4, prior to presenting the conclusions of this work in Section 5.

2. Experimental Set-up

2.1. Wind-tunnel and boundary-layer flow conditions

The experiments were carried out in the Göttingen-type wind tunnel of the Aerospace Engineering Group at the Universidad Carlos III de Madrid. The test section is 1.5 m long with a cross-sectional area of 0.4×0.4 m^2. The maximum wind tunnel speed is 20 m/s, with a high-pass filtered free-stream turbulence intensity below 0.5%.

The turbulent boundary layer was developed on a smooth methacrylate flat plate of 1.25 m length and 10 mm thickness, spanning the entire height of the wind tunnel and located vertically 0.09 m from the wind-tunnel side wall. Throughout this paper x, y, and z are streamwise, wall-normal, and spanwise directions respectively. The mean streamwise, wall-normal, and spanwise velocities are referred to as U, V, and W respectively, while u, v, and w are streamwise, wall-normal, and spanwise velocity fluctuations. The leading edge of the flat plate follows the shape of an ellipse with aspect ratio 5. The origin of the coordinate system in the streamwise direction corresponds to the end of the leading edge. Furthermore, the trailing edge is equipped with a 0.15 m long flap to control the position of the stagnation point. In order to stimulate the transition of the boundary layer to the turbulent regime and fix its location, a tripping device was used. It was composed of a 2.4 mm high turbulator in combination with two DYMO tapes (with the embossed letter V pointing in the flow direction and a nominal height of 0.3 mm). The tripping device was located at $x = 0.05$ m. The method proposed in Ref. [25] has been used to verify that the TBL development was not affected by residual tripping effects in the measurement domain.

The experimental campaign includes testing under three different conditions of pressure gradient, which were obtained by modifying the geometry of one of the test section walls. The modification consisted in using foam sections with converging/diverging inserts that were placed onto the wall opposite to the flat plate, as shown in Fig. 1. For the FPG configuration, the flow was accelerated along the streamwise direction by reducing the tunnel test section height from 0.30 m to 0.27 m along the the full test-section length. The achievable FPG condition was limited by the risk of unsteady separation due to an abrupt flow deceleration in the divergent part of the tunnel. For the APG configuration, the modified wall is composed of two segments. In the first segment the flow was accelerated by reducing the tunnel test section height from 0.30 m to 0.15 m in a length of 0.58 m. In the second segment, an adverse pressure gradient condition was imposed by introducing a divergent section. The shape of the modified wall was designed performing a Reynolds-averaged Navier-Stokes (RANS) simulation, using the SST k-ω turbulence model as in the work by Sanmiguel Vila et al. [22]. For the ZPG configuration, the test section was used in its standard configuration, as described in Ref. [9]. A sketch of the different modified lateral walls used in the present experimental campaign is shown in Fig. 1.

The flat plate was equipped with pressure taps to measure the pressure distribution along it. The pressure taps were separated 0.05 m from each other in the streamwise direction, with the first pressure tap located at $x = 0.025$ m. Using these pressure taps, the pressure distribution is characterized in terms of the pressure coefficient C_p, which is defined for an incompressible flow as:

$$C_p = \frac{P - P_{ref}}{1/2\rho U_{ref}^2} = 1 - \left(\frac{U_\infty}{U_{ref}}\right)^2 , \tag{1}$$

where P is the local static pressure, P_{ref} is the static pres-

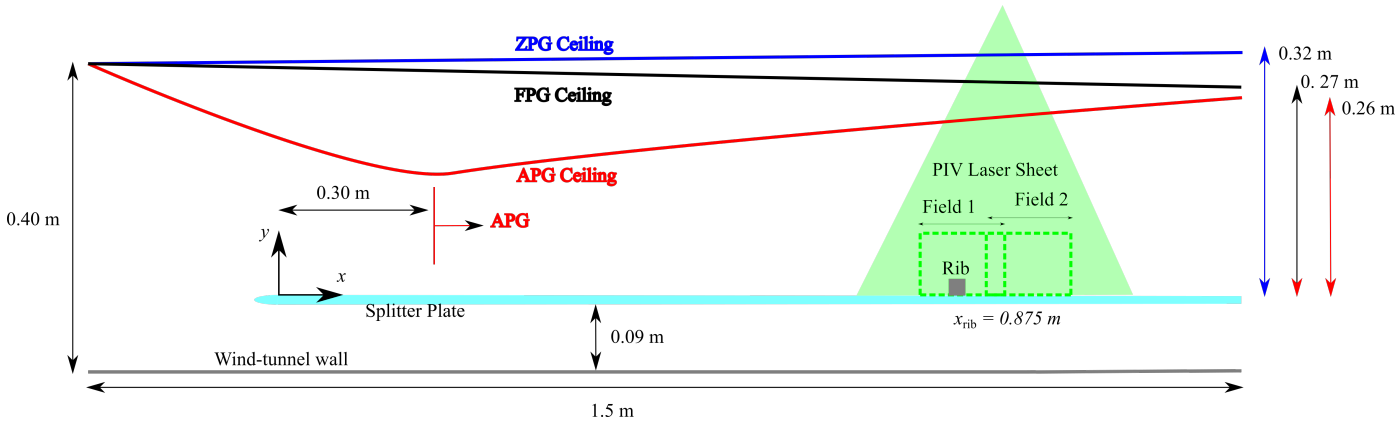

Figure 1: Top-view sketch of the experimental setup. The FPG ceiling is depicted as (——), the ZPG configuration is depicted as (——), and the APG ceiling is depicted as (——). The flat plate is mounted over the non-modified lateral wall by means of bars. The position of the upstream edge of the obstacle is indicated with x_{rib}.

sure in the ZPG region (measured at $x = 0.675$ m), U_∞ is the local free-stream velocity and U_{ref} is the reference free-stream velocity at $x = 0.675$ m. The evolution of C_p along the streamwise direction for the three pressure-gradient configurations is reported in Fig. 2. It is remarked that for the ZPG configuration, a nearly-zero pressure gradient is achieved with very good approximation, with C_p values between -0.025 and 0.025 in the region of interest.

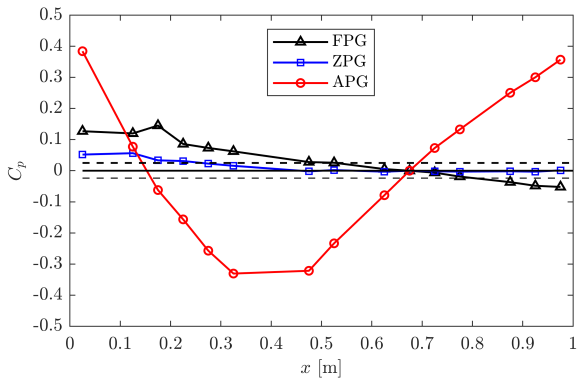

Figure 2: Distribution of pressure coefficient C_p along the streamwise direction. Colours and symbols correspond to the pressure-gradient configurations described in Table 1. Note that the reference pressure for C_p is taken at $x = 0.675$m.

2.2. *Velocity-field measurements*

Velocity-field measurements were performed using PIV in a plane parallel to the freestream, normal to the flat plate, as shown schematically in Fig. 1. The plane was illuminated through the modified wall opposite to the flat plate. Optical access is guaranteed by a small elongated hole in the foam wall, sealed by a transparent plastic window to avoid separation effects. The flow was seeded upstream the tunnel settling chamber using a Laskin nozzle that generates droplets of Di-Ethyl-Hexyl-Sebacate (DEHS) with 1 μm diameter. The seeded flow was illuminated by means of a light sheet of approximately 1 mm thickness, produced by a dual cavity Nd:Yag Quantel Evergreen laser (200mJ/pulse at 10 Hz) and a set of cylindrical and spherical lenses.

Two *ANDOR Zyla sCMOS 5.5MP* cameras (2560 × 2160 pixel array, 6.5μm × 6.5μm pixel size),equipped with a Tokina 100 mm lens, were used to capture PIV images, with a resolution of about 29 pix/mm and a magnification of approximately 0.19. The lens aperture was set to $f/\# = 16$ to ensure avoiding peak locking. The time separation between PIV images was set equal to 20μs for the entire dataset, which corresponds to a freestream displacement of 7-8 pixels, depending on the test case. The cameras and the laser triggers were coordinated by means of a Quantum composer 9520 Series Pulse Delay Generator. An ensemble of 3500 image couples was acquired for both cameras in each pressure-gradient configuration. Laser reflections at the wall and the background were removed using the POD-based approach proposed by Mendez et al. [27].

The PIV image analysis was carried out using a code developed at University of Naples Federico II. The code applies an iterative multi-grid/multi-pass [**?** 28] image deformation algorithm [29] interrogation strategy, with final interrogation windows of 40×40 pixels with 75% overlap. A simplex method and a bilinear interpolation are used respectively for the interpolation of the images and for the dense predictor calculation in the iterative procedure to improve the accuracy [30, 31]. The final vector spacing is equal to 10 pixels, i.e. 0.35 mm, which results in at least 67 vectors throughout the boundary layer thickness in the worst case. The corresponding interrogation-window sizes in inner units are 57×57, 47×47 and 42×42 for the FPG, ZPG and APG cases, respectively.

The mean velocity and the second-order statistics are affected by limited spatial resolution in PIV [32]. To overcome this issue, the Ensemble Particle Tracking Velocimetry (EPTV) approach has been used, with biased search using PIV as a predictor. Bins of 400 × 2 pixels have been used. The resolution of the computed statistics is further improved using the polynomial-fit-based method presented by Agüera et al. [33] and validated in wall-bounded flows in Ref. [23].

The processed images of each camera were merged by using a calibration image taken before each experiment. A calibration target with black dots on a white background is used to establish the field of view of each camera. In the overlap region the velocity vectors have been computed by linear combination of the corresponding vector fields of each camera.

2.3. Statistical characterization of the TBLs

A characterization of the TBLs under pressure gradients without wall-attached ribs has been carried out as a reference case to estimate the boundary-layer parameters. The objective is to determine the corresponding values of β and obtain experiments at matched friction Reynolds number Re_τ (which is defined in terms of the friction velocity u_τ and 99% boundary-layer thickness δ_{99}). The main boundary-layer parameters of the TBLs are presented in Table 1. These quantities are the Clauser pressure-gradient parameter β value, the free-stream velocity U_∞, the Reynolds numbers Re_θ, Re_τ and Re_{δ^*} (based on momentum thickness θ, wall friction velocity u_τ, and displacement thickness δ^* respectively), the boundary-layer thickness δ_{99}, and the shape factor H_{12}. Note that the absolute value of the Clauser parameter β computed for the ZPG case is below 0.005, which is considered to be low enough to be representative of ZPG conditions although the C_p curve is not exactly zero. In this work, the composite profile reported in Ref. [34] was used to deduce the absolute wall position and the friction velocity; this method has been shown to be robust whenever near-wall measurements are at hand [35, 36, 37] and enhancing the accuracy of measurements techniques in high Reynolds number TBLs for more representative comparison to their canonical representations. To this end, EPTV measurements allowed to obtain a sufficiently large number of points within the sublayer and buffer region in order to correct for the absolute wall position and determine the friction velocity without relying on log-law constants. Only points up to $y^+ = 30$ are considered, where deviations from the law of the wall are negligible for the relatively low absolute value of β of the FPG and APG cases.

It is worth noting that, even if in the FPG case the boundary layers develops under the effect of a significant pressure gradient (the C_p is in absolute value only about one half of that of the APG case in the measurement location), the magnitude of β is much smaller than in the APG case. This should not surprise since under a favourable pressure gradient the skin-friction coefficient is enhanced and the displacement thickness is reduced, thus resulting in a smaller β. This might anticipate much less significant discrepancies with the ZPG case than in the APG case.

In Fig. 3 a comparison between inner-scaled turbulence statistics for the three values of β at matched friction Reynolds number Re_τ is reported. The mean velocity profiles of the three cases collapse from the wall up to $y^+ \approx 150$, thus showing no significant discrepancy with the law of the wall [22, 38] for these relatively mild pressure-gradient conditions. As expected, the APG case shows a more prominent wake than the corresponding ZPG and FPG cases. This behaviour is produced by the reduced wall-shear stress present in APGs, which is connected to the increased wall-normal convection. Due to the limited strength of the FPG conditions, the FPG profile shows little deviation from the ZPG profile.

The streamwise Reynolds stress indicates the emergence of an outer peak at $y^+ \approx 200$ for the APG case, which is not present in the ZPG and FPG cases. This increase of the inner-scaled streamwise Reynolds stresses is not just due to the lower value of the friction velocity used to scale the profile, but it is produced by large-scale motions in the outer region [39]. Additionally, this peak can be observed more profoundly in the Reynolds wall-normal and shear stress profiles. Apart from that, the inner-peak intensity for the streamwise variance is strengthened in the APG profile as a result of the inner/outer interaction [22].

For each case, a rib has been placed at the same streamwise location where the characterization has been carried out. The selected rib geometry is a square cylinder and it spans for the complete width of the flat plate. The ratio k/δ_{99} is set to ≈ 0.35 for each pressure gradient, where k is the rib height reported in Table 2. Owing to the choice of the flow cases with matched Re_τ and matched k/δ_{99}, the rib height takes the same value both in inner and outer scaling for all the tested configurations, thus allowing to isolate the effects due to the pressure gradient.

3. Results

3.1. Mean velocity fields

The mean velocity fields for the three cases obtained from the PIV measurements are shown in Fig. 4 with superposed streamlines. The streamwise velocity is normalised with the free-stream velocity U_∞ of the corresponding conditions without rib (reported in Table 1). Regions which were not optically accessible due to the presence of the obstacle and due to the laser light attenuation through the modified lateral wall are blanked.

Regarding the flow upstream of the rib, the location of the mean stagnation point ($\overline{y_0}/k$) is shifted upwards with increasing β. This is ascribed to the reduced wall friction due to the pressure gradient, which promotes the lifting up of the near-wall region. The influence of the inflow conditions on the location of the stagnation point was discussed by Vinuesa et al. [40], in particular the difference between laminar and turbulent incoming boundary layers. The flow then separates from the top of the obstacle, generating a shear layer with a distinct shedding signature. Streamwise velocity spectra are computed at different heights to investigate the effect of the pressure gradient on its development. Table 2 reports the height of the position where a peak in the spectra is observed. The uncertainty is computed considering the range described by the points in which the spectrum reaches a value equal to 95% of its maximum value. The wall-normal distance of the maximum position is practically independent of β when scaled in outer units, and located at $y/\delta_{99} \approx 0.6$. On the other hand, the dominant non-dimensional shedding frequency, expressed as Strouhal number $St = k/l$ (with l being the wavelength corresponding to the maximum of the spectrum) increases with the β value. The observed result for the ZPG configuration is in line with the values reported by Hearst et al. [11] for cube obstacles. It has to

Table 1: Boundary-layer (without rib) parameters of the various cases in the present experimental database.

Case	β	U_∞ [m/s]	Re_θ	Re_τ	Re_{δ^*}	δ_{99} [mm]	H_{12}	Symbol
FPG	−0.12	14.69	2280	960	3200	23	1.37	(△)
ZPG	∼ 0	12.71	2150	860	3000	25	1.39	(□)
APG	1.2	13.76	3390	870	5200	27	1.50	(○)

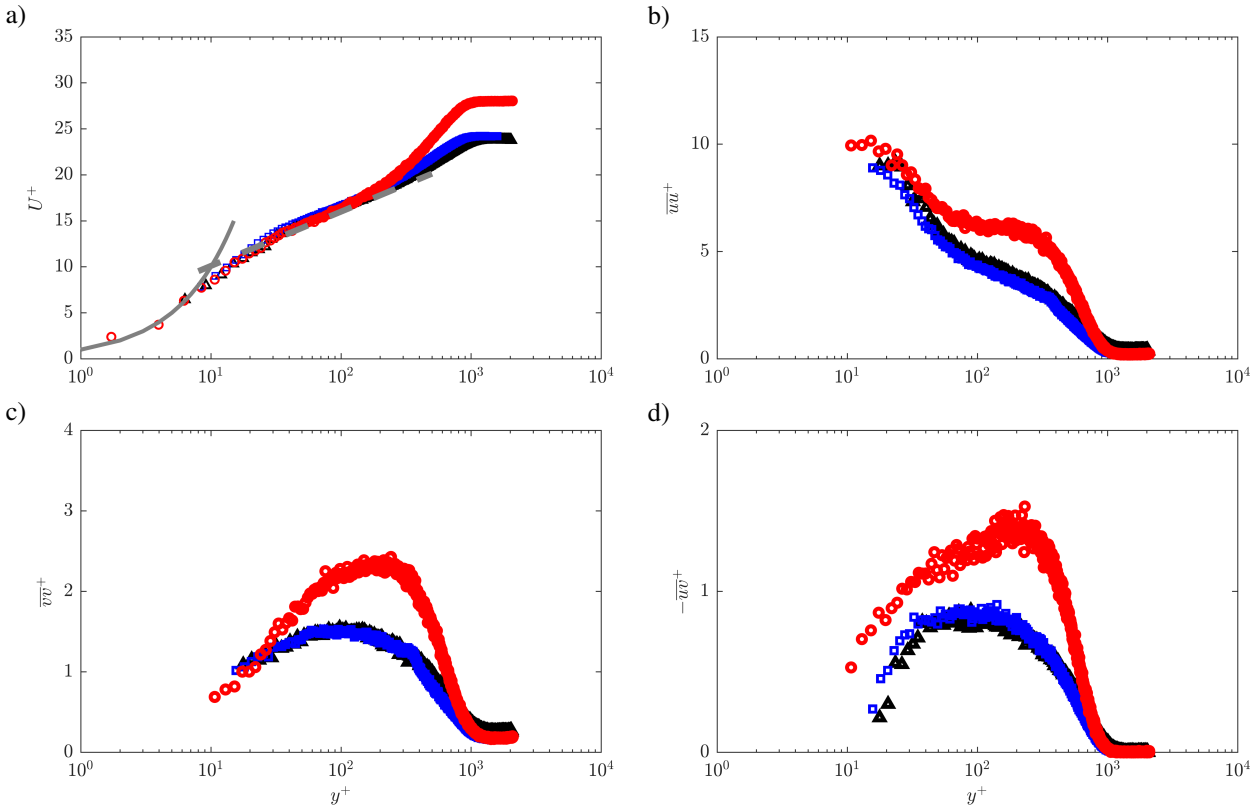

Figure 3: Inner-scaled (a) mean streamwise velocity, (b) streamwise Reynolds stress, (c) wall-normal Reynolds stress and (d) Reynolds shear stress. Colours and symbols correspond to the pressure-gradient configurations described in Table 1. Additionally, (a) shows the linear profile $U^+ = y^+$ (——) and the logarithmic profile $U^+ = ln(y^+)/0.41 + 5.2$ (− −) with the low-Re logarithmic law constants.

be remarked that with the available dataset we are able to retrieve spatial frequencies of the shedding, while the convection velocity of the shed vortices is not known. The definition of the Strouhal number used in this work implicitly assumes that the convection velocity is equal to the free-stream velocity and that it does not evolve in the streamwise direction. While this assumption is supported by the good agreement with the ZPG results of Hearst et al. [11], the differences for APG and FPG could also be ascribed to the difficulty of defining a convection velocity when the flow is evolving in the streamwise direction (especially in the APG case where a stronger deceleration is found in the test section) [39].

In all the cases under study, a recirculation bubble with length larger than 10 times the height of the obstacle is observed. Note that the reattachment point of the recirculation bubble is computed as the location of sign change from negative to positive mean streamwise velocity. It is interesting to note that the recirculation bubble increases in size when increasing β. This behaviour differs from the one found in turbulent channels, where the recirculation region center was observed to be almost independent of the pressure gradient [18]. The mean reattachment point of this region, found by visual inspection of Fig. 4, is reported in Table 2. The reattachment length of the ZPG case is larger than past cubes [11], reaching more similar values to those observed by Ra and Chang [15] for backward-facing steps. For the APG case it was not possible to identify the reattachment point due to the limited field of view when scaled in outer units. Indeed, while the physical field of view is the same for the three cases, its size in outer units (and thus when scaled with the obstacle height, having fixed k/δ_{99}) changes depending on δ_{99}, which is larger for the APG case due to pressure-gradient effect. Nonetheless, the topology of the streamlines supports the picture that the reattachment length increases with increasing β. This effect can be explained by the increase of

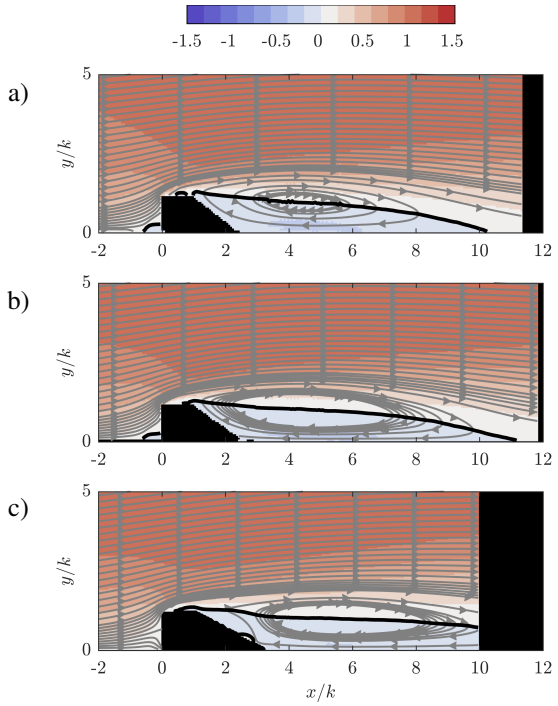

Figure 4: Mean streamwise velocity fields U/U_∞ against the normalized wall-normal direction, y/k. From top to bottom: a) FPG, b) ZPG, and c) APG. Grey lines represent the flow streamlines and the solid black line represents the demarcation to the separated region. Areas in the final part of the image in which the laser illumination was not sufficient are blanked in black color.

wall-normal convection due to the adverse pressure gradient.

It is worth noting here that, as expected due to the small β value obtained, the case under FPG presents very minor differences with respect to the ZPG case. This result supports the observation that β is very relevant when analyzing the effect on the local flow organization.

It has to be remarked here that the pressure-gradient increase affects the fluctuating velocity profile, as it can be seen in Fig. 3. This determines a different turbulence intensity profile upstream of the obstacle. Hearst et al. [11] report that the wake length is decreased when increasing the turbulence intensity level, while here it is shown that when the streamwise velocity fluctuation at the obstacle height is increased with the pressure gradient, the wake becomes longer. Note that Vinuesa et al. [40] also reported a connection between higher streamwise velocity fluctuations at the obstacle location and length of the wake behind the obstacle. Consequently, the present data supports a picture in which the turbulence intensity level at the obstacle height has a weaker effect than that of the pressure gradient.

3.2. Turbulence statistics

The turbulence statistics for the three test cases are reported in Fig. 5 at several positions upstream ($x/k = -2$) and downstream ($x/k = [2, 4, 6, 8]$) the rib. Data are represented in non-dimensional form using outer scaling, i.e. U/U_e, $\overline{uu}/U_e^2$, $\overline{vv}/U_e^2$ and $\overline{uv}/U_e^2$, with U_e being the velocity outside of the boundary layer at the corresponding streamwise location.

Table 2: Characteristics of the flow in the immediate proximity of the wall-mounted rib. From left to right, the columns indicate: the test case; the rib height k; the mean reattachment point $\overline{x_r}/k$; the wall-normal position of the front stagnation point of the rib $\overline{y_0}/k$; the Strouhal number St and the wall-normal position y_{St}/δ_{99} of the peak of the streamwise velocity spectrum.

Case	k [mm]	$\overline{x_r}/k$	$\overline{y_0}/k$	St	y_{St}/δ_{99}
FPG	8.3	10.1	$\sim$	0.11	0.64 ± 0.05
ZPG	9.1	11.1	0.55	0.12	0.61 ± 0.05
APG	10.8	$\sim$	0.64	0.15	0.67 ± 0.04

The mean streamwise velocity profiles reported in Fig. 5 show evidence of the large impact that ribs have on the flow field behind them. The flow detaches from the wall and requires several rib lengths to reattach. Regarding the effect of β, it is seen that the increase of adverse pressure gradient moves significantly downstream the reattachment point. In terms of streamwise Reynolds stresses, from Fig. 5 it can be noticed that the rib presence leads to the generation in its wake of a strong fluctuation intensity peak which outclasses the inner peak present close to the wall ($y^+ \approx 15$) in the streamwise Reynolds stress profile before the rib. This peak becomes dominant in the wake, and according to the literature [41] the TBLs needs much more distance to recover its canonical state than to reattach to the wall. Cutler and Johnston [41] show that even for measurements at $x/k > 80$ the APG TBL canonical shape was not recovered. In the present study it was possible to obtain measurements for the three β cases up to $y/k = 8$, and at that position no reduction of the outer peak intensity can be observed. The origin of this outer peak is addressed to the shedding from the rib leading edge. For what concerns the β effect, it cannot be appreciated immediately. It has been shown in the literature [18] that the flow features in the immediate region downstream of the rib are dominated by the rib effects itself, while further downstream the pressure gradient starts to affect the wake development. While at $x/k = 2$ and $x/k = 4$ the peaks of the three pressure gradient cases collapse at $y/\delta_{99} \approx 0.6$ ($y/k \approx 2$), further downstream the increase of β makes the peak wider in the wall-normal direction. This is similar to the well-known effect of β in canonical TBLs, where a secondary peak is created further from the wall. In any case, these two peaks must not be confused, as their origin, position and intensity are completely different. Additionally, the intensity of the peak is attenuated for increasing β.

The effect of the rib on the Reynolds wall-normal and shear stresses is similar to that on the streamwise Reynolds stresses. An outer peak is generated at $y/\delta_{99} \approx 0.6$ ($y/k \approx 2$) and is not immediately affected by the pressure gradient until further downstream. In any case, the increase of intensity of both Reynolds wall-normal and shear stresses is significantly larger than for the streamwise counterpart.

In order to provide further insight on the effect of the pressure gradient on the wake development, Fig. 6 reports the wall-normal position of $U = 0.8U_e$ and of the maximum of the streamwise Reynolds normal stress. As remarked previously,

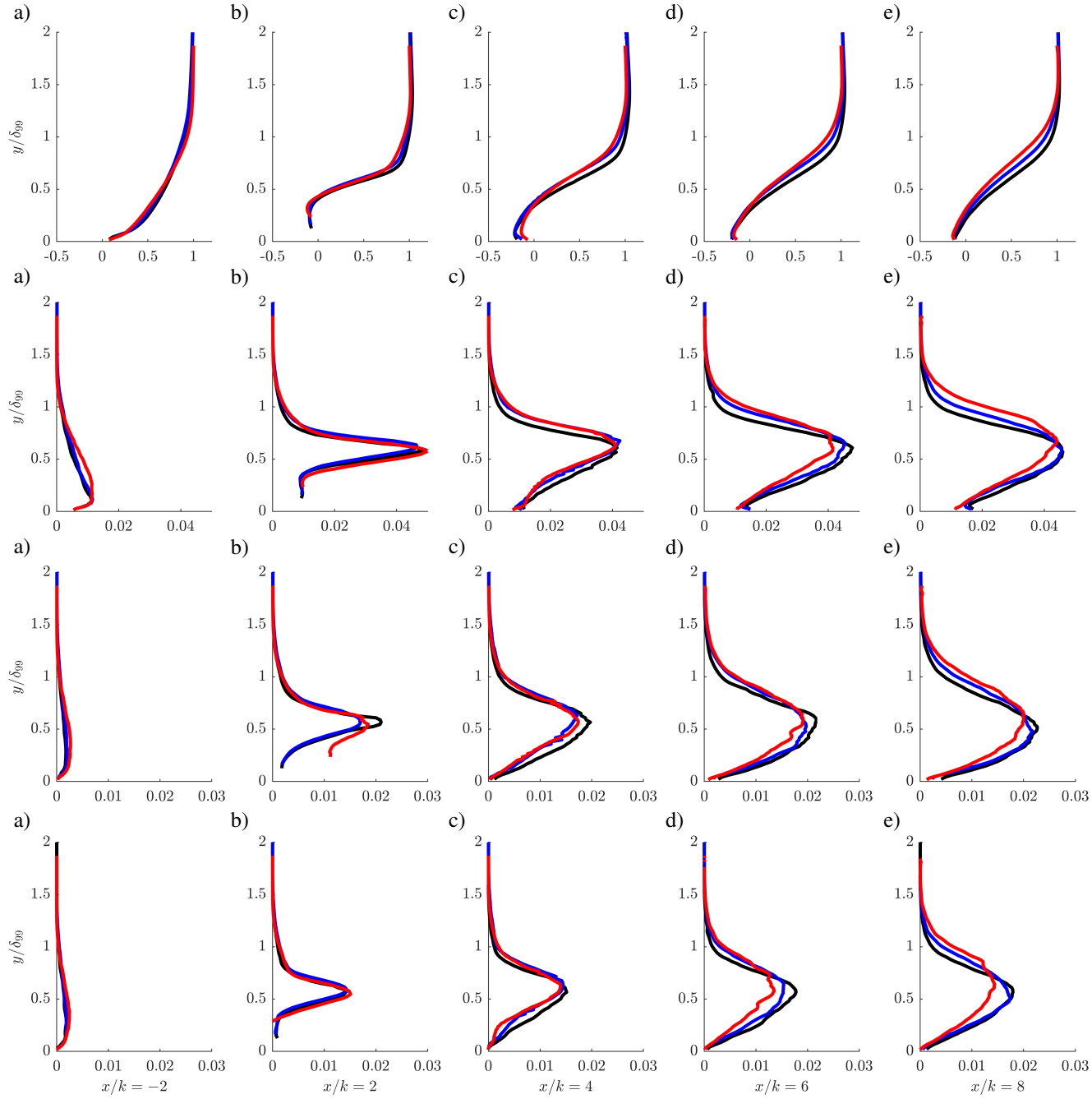

Figure 5: Turbulence statistics profiles at several positions upstream and downstream of the rib. The columns indicate the distance from the leading edge of the obstacles, going in steps of $2k$. The rows are U/U_e, $\overline{uu}/U_e^2$, $\overline{vv}/U_e^2$ and $\overline{uv}/U_e^2$ from top to bottom. The colours correspond to the pressure-gradient configurations described in Table 1.

notwithstanding the large difference in pressure coefficient, the differences between the ZPG and the FPG cases are almost negligible, thus further confirming that β is a more meaningful parameter to characterize pressure-gradient effects for ribs in TBLs. For the case of the APG the velocity defect behind the obstacle increases more rapidly, owing to the reduced skin-friction coefficient due to the action of the pressure gradient. The position of the maximum streamwise normal Reynolds stress is less affected by the pressure gradient, with a weaker increase of the wall-normal distance for the APG case with respect to ZPG and FPG case, which is observed only at $x/k > 5$. This is indicative of the dominance of the shear induced by the obstacle in determining the production of turbulent kinetic energy in the wake.

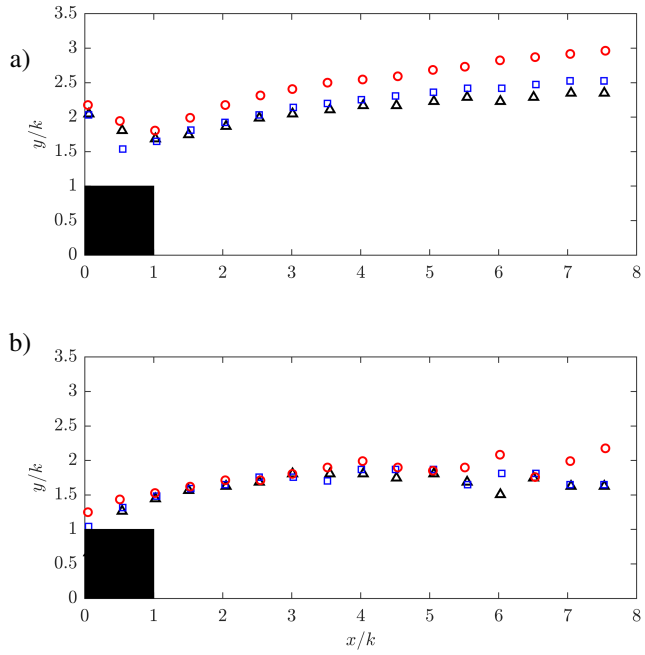

Figure 6: Evolution of the vertical position along the streamwise direction of (a) $U = 0.8U_e$, and (b) $\overline{uu}_{max}$. Colours and symbols correspond to the pressure-gradient configurations described in Table 1.

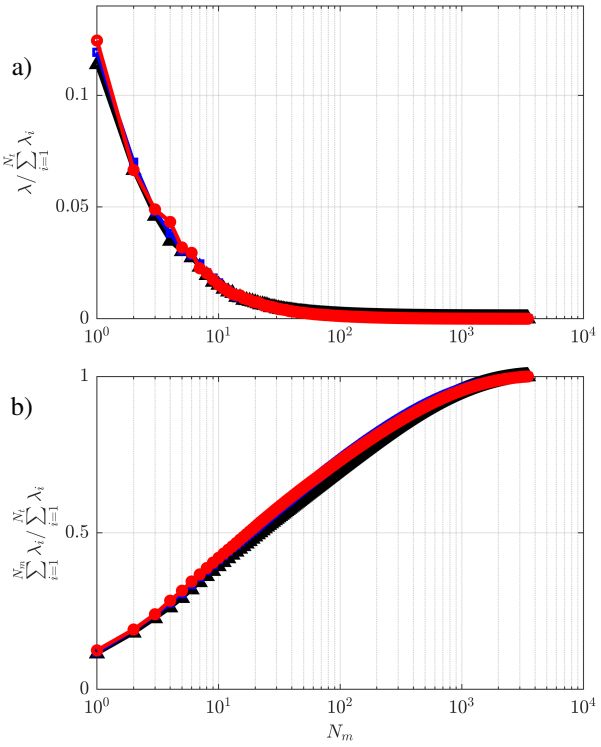

Figure 7: (a) shows the POD spectrum of the eigenvalues λ_i and (b) cumulative sum of the eigenvalues. Colours and symbols correspond to the pressure-gradient configurations described in Table 1.

4. POD modal analysis

In order to perform a modal decomposition of the flow fields under investigation, the POD snapshots approach [42] was employed. After subtracting the mean, fluctuating velocity fields were rearranged in form of snapshot matrices for both streamwise $\underline{\underline{u}}$ and wall-normal $\underline{\underline{v}}$ velocity components. Such snapshot matrices have a size $N_t \times N_p$, with N_t being the number of snapshots and N_p the number of grid points of the field.

$$\underline{\underline{u}} = \begin{bmatrix} u(x_1,t_1) & \dots & u(x_{N_p},t_1) \\ \vdots & \ddots & \vdots \\ u(x_1,t_{N_t}) & \dots & u(x_{N_p},t_{N_t}) \end{bmatrix}, \tag{2}$$

$$\underline{\underline{v}} = \begin{bmatrix} v(x_1,t_1) & \dots & v(x_{N_p},t_1) \\ \vdots & \ddots & \vdots \\ v(x_1,t_{N_t}) & \dots & v(x_{N_p},t_{N_t}) \end{bmatrix}. \tag{3}$$

POD modes are obtained from the singular-value decomposition of the temporal correlation matrix

$$\underline{\underline{C}} = \underline{\underline{u}}\underline{\underline{u}}^T + \underline{\underline{v}}\underline{\underline{v}}^T = \underline{\underline{\Psi}}\underline{\underline{\Lambda}}\underline{\underline{\Psi}}^T, \tag{4}$$

where ^{T} refers to a matrix transpose. The matrix $\underline{\underline{\Psi}}$ contains the temporal modes while the matrix $\underline{\underline{\Lambda}}$ is a diagonal matrix containing the eigenvalues of the correlation matrix, which correspond to the turbulent kinetic energy content of each mode. Spatial modes can then be obtained through:

$$\begin{aligned} \underline{\underline{\Phi_u}} &= \underline{\underline{\Lambda}}^{-\frac{1}{2}}\underline{\underline{\Psi}}^T\underline{\underline{u}} \\ \underline{\underline{\Phi_v}} &= \underline{\underline{\Lambda}}^{-\frac{1}{2}}\underline{\underline{\Psi}}^T\underline{\underline{v}}. \end{aligned} \tag{5}$$

where $\underline{\underline{\Lambda}}^{-\frac{1}{2}}$ is a diagonal matrix containing in its diagonal the inverse of the square root of the elements in the diagonal of $\underline{\underline{\Lambda}}$.

Fig. 7 reports the energy distribution among the POD modes, i.e. the elements on the diagonal of $\underline{\underline{\Lambda}}$, for the test cases with ribs. The eigenvalues of the two-point correlation matrix, representative of the energy content of the modes, are normalized with their sum, thus representing a normalized contribution to the total turbulent kinetic energy. The results for the cases without ribs are not reported for brevity, and are substantially in line with Ref. [23]. The energy distribution of the POD modes appears unaffected by β, in agreement with Shah and Tachie [19]. A reduction of energy for the first modes is observed if compared with the corresponding APG conditions without ribs [23], where the first mode contains approximately 16% of the energy. This can be ascribed to the disruptive effect of the ribs on the highly energetic large-scale motions (LSMs) usually observed in the first POD modes of wall-bounded flows [23, 43, 44, 45].

The contour of the streamwise component of the first four

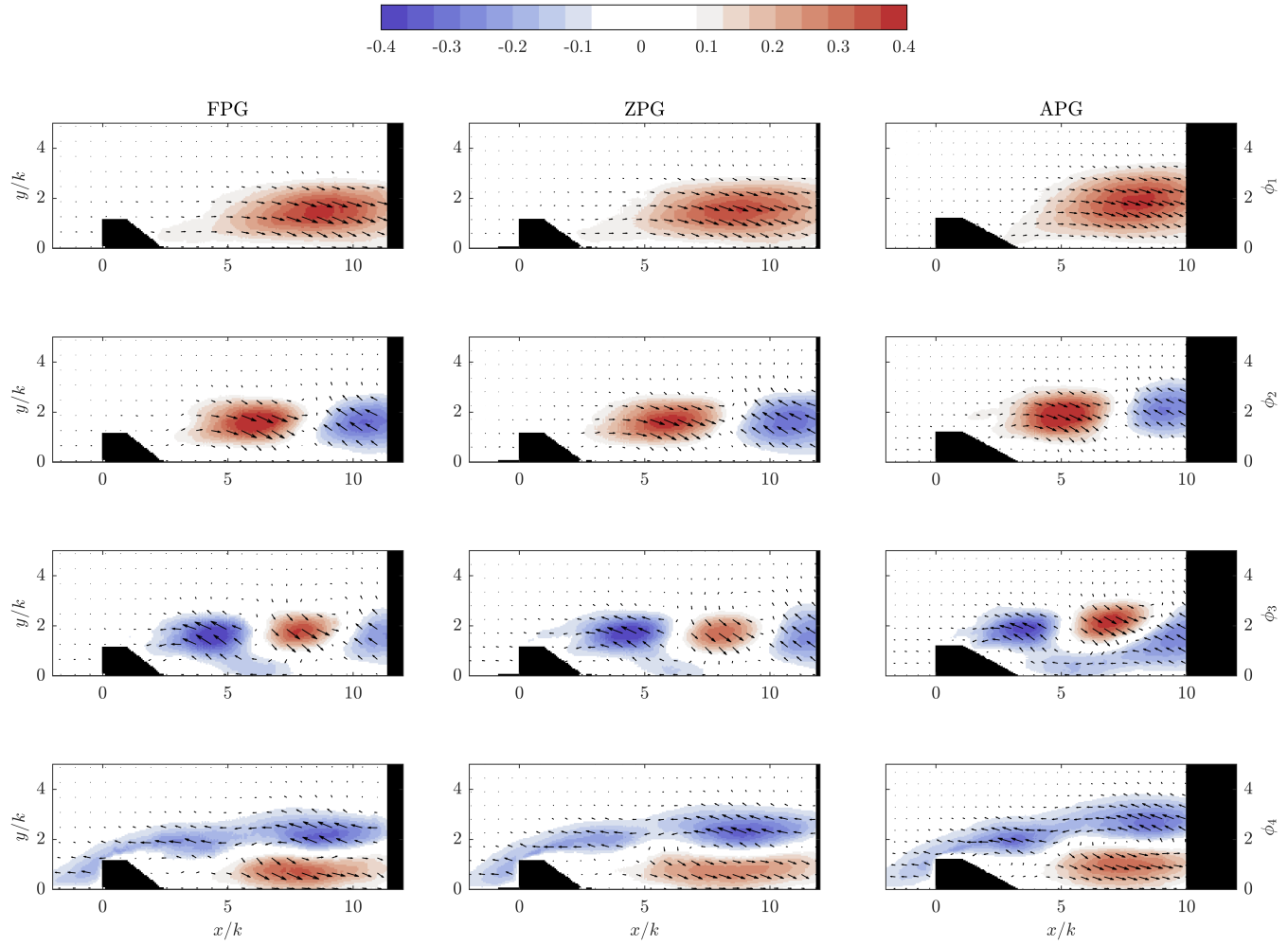

Figure 8: Colour plots of the streamwise component of the POD spatial modes for FPG (left column), ZPG (center column), and APG (right column) cases. The rows indicate ϕ_1 (first row), ϕ_2 (second row), ϕ_3 (third row), and ϕ_4 (fourth row). The modes are scaled to unit energy in the full domain. Areas in the final part of the image in which the laser illumination was not sufficient are blanked in black color.

spatial POD modes for the three β cases is reported in Fig. 8. The spatial modes for the corresponding conditions without ribs are not included here for brevity, and are in substantial agreement with Refs. [9, 43] for the ZPG case and with Ref. [23] for the APG case. A detailed discussion of how the modes in canonical ZPG and APG TBLs are organised can be found in Refs. [23, 43].

The central column of Fig. 8 reports the four most energetic modes of the ZPG case, which are in line with the modes reported by Mallor et al. [9] in similar conditions. It has to be noted that the first four spatial modes for the wall-mounted ribs seem to be not coupled, i.e. they do not show flow features with the same wavelength. Nonetheless, their combination seems to capture the vortical structures at the shear layer created by the rib, i.e. the Kevin-Helmholtz instabilities that are produced. These structures result in spanwise eddies that characterise the outer region of the rib wake. The effect of these eddies has been also shown in the *uv* profiles reported at Fig. 5, which are much more dominant than the two other Reynolds stresses. A similar study was performed by **?**], but only the first three modes are in line with the results presented here. The discrepancy in the fourth mode can be attributed to the different k/δ_{99} ratios: higher values of this ratio lead to a more prominent effect of the vortical structures shed from the rib on the boundary layer.

Regarding the pressure-gradient effect, the previous section showed that its introduction affects significantly both the mean velocity field and the Reynolds stresses, and it is expected that it should also affect the characteristics of the spatial POD modes. The spatial POD modes for different β values are reported in Fig. 8. The analysis of Fig. 8 going from the left to the right for increasing β allows to identify this effect on the most energetic flow features. Again, small differences can be observed between APG and ZPG cases, due to the small absolute value of β experienced by the flow. With increasing β, however, it can be seen that the main structures present in the modes are displaced farther from the wall but their spatial wavelength and characteristic organization barely change. The displacement of the high-energy-content features toward the outer layer might be

advantageous due to their ability to bring more high-momentum fluid towards the wall and at the same time providing reduced skin-friction effect on the wall. This statement, requires, however, caution, since, according to our recent findings in Ref. [46] near-wall coherent eddies are very effective in enhancing wall heat transfer thus further studies are required to verify whether APG might be beneficial or not for heat transfer enhancement purposes.

5. Conclusions

An experimental study of wall-attached ribs in turbulent boundary layers developing under the effect of a pressure gradient has been carried out. The experiments were conducted at matched friction Reynolds number and height of the obstacle normalized with the boundary-layer thickness. This choice allows the authors to obtain the same obstacle height for the three cases (FPG, ZPG and APG) both in inner and outer scaling, thus isolating the pressure-gradient effects from Reynolds-number and obstacle-height effects.

It has been shown that, to estimate the significance of pressure-gradient effects on the development of the wake behind the ribs, a non-dimensional expression that quantifies the relative importance of the forces due to the local pressure gradient and shear stress is a much more suitable parameter than the pressure coefficient itself. While there is only a factor of 2 between the magnitudes of the pressure coefficients from the FPG and APG cases, the discrepancy with the ZPG case in terms of flow field organization and turbulent statistics is much more significant for the APG case. In particular, the Clauser pressure-gradient parameter is proposed here as a suitable non-dimensional parameter. This is well reflected by the large difference in the β magnitude between the two cases. The use of only three flow cases at a fixed Reynolds number, however, does not allow to draw a general conclusion for any value of the pressure gradient and of the Reynolds number. Thus there is a clear need for further investigations on the meaningfulness of other non-dimensional pressure-gradient parameters available in the literature such as, for instance, the pressure gradient expressed in inner units $(dp/dx)^+$, the acceleration parameter K or the accumulated Clauser pressure-gradient parameter $\overline{\beta}$ [13].

The results show that an adverse pressure gradient has the effect of increasing the momentum defect behind the obstacle, thus pushing the boundary-layer edge farther away from the wall. Even though much weaker, this effect is also observed on the peak of the streamwise Reynolds stress. The peak width increases for both streamwise and wall-normal velocity variance, possibly due to an interaction with the outer peak observed in APG TBLs [22]. The recirculation bubble is also longer in the APG case, thus leading to delayed flow reattachment.

In line with the observations on the mean flow features, the effects of the pressure gradient on the flow structure are prominent in the APG case. This further supports the suitability of the Clauser pressure-gradient parameter as a possible option for assessing the pressure-gradient significance in the development of the wake of wall-attached ribs. The coherent features in the fluctuating part of the flow field are very similar among the cases with and without pressure gradient. As observed in the literature (see, e.g. Refs. [8, 9]) the flow field downstream of the rib is characterized by Kelvin–Helmholtz features which develop in the shear layer at the edge of the separated region. Also the relative energy contribution of the modes is practically unchanged by the pressure gradient in the investigated range. The main differences are observed under the effect of an adverse pressure gradient which advects the coherent eddies farther from the wall. The impact of the APG conditions on the flow, displacing coherent eddies towards the outer layer, possibly resulting in reduced wall-shear stress without penalizing the convective heat transfer at the wall, should be object of future research including detailed heat-transfer measurements.

Acknowledgements

CSV, SD, AI, RÖ and PS were partially supported by the Grant DPI2016-79401-R funded by the Spanish State Research Agency (SRA) and European Regional Development Fund. RÖ, RV and PS acknowledge the financial support from the Knut and Alice Wallenberg (KAW) Foundation as part of the Wallenberg Academy Fellow programme and the Lundeqvist foundation.

References

[1] S. V. Garimella, L.-T. Yeh, T. Persoons, Thermal management challenges in telecommunication systems and data centers, IEEE Trans. Components, Packaging and Manufacturing Technology 2 (2012) 1307–1316.

[2] J.-C. Han, S. Dutta, S. Ekkad, Gas turbine heat transfer and cooling technology, CRC Press, 2012.

[3] M. Dalle Donne, L. Meyer, Turbulent convective heat transfer from rough surfaces with two-dimensional rectangular ribs, Int. J. Heat Mass Transfer 20 (1977) 583–620.

[4] J.-C. Han, L. Glicksman, W. Rohsenow, An investigation of heat transfer and friction for rib-roughened surfaces, Int. J. Heat Mass Transfer 21 (1978) 1143–1156.

[5] J. Park, J. Han, Y. Huang, S. Ou, R. Boyle, Heat transfer performance comparisons of five different rectangular channels with parallel angled ribs, I. J. Heat Mass Transfer 35 (1992) 2891–2903.

[6] T.-M. Liou, J.-J. Hwang, S.-H. Chen, Simulation and measurement of enhanced turbulent heat transfer in a channel with periodic ribs on one principal wall, Int J. Heat Mass Transfer 36 (1993) 507–517.

[7] X. Gao, B. Sunden, Heat transfer and pressure drop measurements in rib-roughened rectangular ducts, Exp. Thermal Fluid Sci. 24 (2001) 25–34.

[8] C. He, Y. Liu, D. Peng, S. Yavuzkurt, Measurement of flow structures and heat transfer behind a wall-proximity square rib using tsp, piv and split-fiber film, Exp. Fluids 57 (2016) 165.

[9] F. Mallor, M. Raiola, C. S. Vila, R. Örlü, S. Discetti, A. Ianiro, Modal decomposition of flow fields and convective heat transfer maps: An application to wall-proximity square ribs, Exp. Thermal Fluid Sci. 102 (2019) 517–527.

[10] I. P. Castro, E. Epik, Boundary layer development after a separated region, J. Fluid Mech. 374 (1998) 91–116.

[11] R. J. Hearst, G. Gomit, B. Ganapathisubramani, Effect of turbulence on the wake of a wall-mounted cube, J. Fluid Mech. 804 (2016) 513–530.

[12] T. Houra, Y. Nagano, Effects of adverse pressure gradient on heat transfer mechanism in thermal boundary layer, Int. J. Heat Fluid Flow 27 (2006) 967–976.

[13] R. Vinuesa, R. Örlü, C. S. Vila, A. Ianiro, S. Discetti, P. Schlatter, Revisiting history effects in adverse-pressure-gradient turbulent boundary layers, Flow, Turbul. Combust. 99 (2017) 565–587.

[14] D. A. D. Kuehn, Effects of adverse pressure gradient on the incompressible reattaching flow over a rearward-facing step, AIAA J. 18 (1980) 343–344.

[15] S. H. Ra, P. K. Chang, Effects of pressure gradient on reattaching flow downstream of a rearward-facing step, J. Aircraft 27 (1990) 93–95.
[16] D. M. Driver, H. L. Seegmiller, Features of a reattaching turbulent shear layer in divergent channelflow, AIAA J. 23 (1985) 163–171.
[17] M. K. Shah, M. F. Tachie, Flow relaxation past a transverse square rib in pressure gradients, AIAA J. 46 (2008) 1849–1863.
[18] M. K. Shah, M. F. Tachie, Piv investigation of flow over a transverse square rib in pressure gradients, J. Turbulence 10 (2009) N39.
[19] M. K. Shah, M. F. Tachie, Proper orthogonal decomposition analysis of separated and reattached pressure gradient flows, AIAA J. 47 (2009) 2616–2631.
[20] F. H. Clauser, Turbulent boundary layers in adverse pressure gradients, J. Aero. Sci. 21 (1954) 91–108.
[21] A. A. Townsend, The structure of turbulent shear flow, Cambridge university press, 1956.
[22] C. Sanmiguel Vila, R. Vinuesa, S. Discetti, A. Ianiro, P. Schlatter, R. Örlü, Large-scale motions and amplitude modulation in adverse-pressure-gradient turbulent boundary layers, J. Fluid Mech. submitted (2019).
[23] C. Sanmiguel Vila, R. Örlü, R. Vinuesa, P. Schlatter, A. Ianiro, S. Discetti, Adverse-pressure-gradient effects on turbulent boundary layers: statistics and flow-field organization, Flow, Turbul. combustion 99 (2017) 589–612.
[24] J. Monty, Z. Harun, I. Marusic, A parametric study of adverse pressure gradient turbulent boundary layers, International Journal of Heat and Fluid Flow 32 (2011) 575–585.
[25] C. Sanmiguel Vila, R. Vinuesa, S. Discetti, A. Ianiro, P. Schlatter, R. Örlü, On the identification of well-behaved turbulent boundary layers, J. Fluid Mech. 822 (2017) 109–138.
[26] R. Vinuesa, P. H. Rozier, P. Schlatter, H. M. Nagib, Experiments and computations of localized pressure gradients with different history effects, AIAA Jo 52 (2014) 368–384.
[27] M. Mendez, M. Raiola, A. Masullo, S. Discetti, A. Ianiro, R. Theunissen, J.-M. Buchlin, Pod-based background removal for particle image velocimetry, Exp. Thermal Fluid Sci. 80 (2017) 181–192.
[28] J. Soria, An investigation of the near wake of a circular cylinder using a video-based digital cross-correlation particle image velocimetry technique, Exp. Thermal Fluid Sci. 12 (1996) 221–233.
[29] F. Scarano, Iterative image deformation methods in piv, Meas. Sci. Technol. 13 (2001) R1.
[30] T. Astarita, G. Cardone, Analysis of interpolation schemes for image deformation methods in PIV, Exp. Fluids 38 (2005) 233–243.
[31] T. Astarita, Analysis of interpolation schemes for image deformation methods in PIV: effect of noise on the accuracy and spatial resolution, Exp. Fluids 40 (2006) 977–987.
[32] C. J. Kähler, S. Scharnowski, C. Cierpka, On the resolution limit of digital particle image velocimetry, Experiments in Fluids 52 (2012) 1629–1639.
[33] N. Agüera, G. Cafiero, T. Astarita, S. Discetti, Ensemble 3d ptv for high resolution turbulent statistics, Meas. Sci. Technol. 27 (2016) 124011.
[34] K. A. Chauhan, P. A. Monkewitz, H. M. Nagib, Criteria for assessing experiments in zero pressure gradient boundary layers, Fluid Dyn. Res. 41 (2009) 021404.
[35] R. Örlü, J. H. M. Fransson, P. H. Alfredsson, On near wall measurements of wall bounded flows – the necessity of an accurate determination of the wall position, Prog. Aero. Sci. 46 (2010) 353–387.
[36] E. Rodríguez-López, P. J. K. Bruce, O. R. H. Buxton, A robust post-processing method to determine skin friction in turbulent boundary layers from the velocity profile, Exp. Fluids 56 (2015) 68.
[37] R. Vinuesa, H. M. Nagib, Enhancing the accuracy of measurement techniques in high Reynolds number turbulent boundary layers for more representative comparison to their canonical representations, European Journal of Mechanics-B/Fluids 55 (2016) 300–312.
[38] P. Bradshaw, G. P. Huang, The law of the wall in turbulent flow, Proc. R. Soc. Lond. A 451 (1995) 165–188.
[39] Z. Harun, J. P. Monty, R. Mathis, I. Marusic, Pressure gradient effects on the large-scale structure of turbulent boundary layers, J. Fluid Mech. 715 (2013) 477–498.
[40] R. Vinuesa, P. Schlatter, J. Malm, C. Mavriplis, D. S. Henningson, Direct numerical simulation of the flow around a wall-mounted square cylinder under various inflow conditions, J. Turbul. 16 (2015) 555–587.
[41] A. D. Cutler, J. P. Johnston, The relaxation of a turbulent boundary layer in an adverse pressure gradient, J. Fluid Mech. 200 (1989) 367–387.
[42] L. Sirovich, Turbulence and the dynamics of coherent structures. ii. symmetries and transformations, Quarterly of Applied mathematics 45 (1987) 573–582.
[43] Y. Wu, A study of energetic large-scale structures in turbulent boundary layer, Phys. Fluids 26 (2014) 045113.
[44] Y. Wu, K. Christensen, Spatial structure of a turbulent boundary layer with irregular surface roughness, J. Fluid Mech. 655 (2010) 380–418.
[45] S. Discetti, B. G, R. Örlü, J. Serpieri, C. Sanmiguel Vila, M. Raiola, X. Zheng, L. Mascotelli, A. Talamelli, A. Ianiro, Characterization of very-large-scale motions in high-*re* pipe flows, Expe. Thermal Fluid Sci. in press (2019).
[46] F. Mallor, C. S. Vila, A. Ianiro, S. Discetti, Wall-mounted perforated cubes in a boundary layer: Local heat transfer enhancement and control, Int. J. Heat Mass Transfer 117 (2018) 498–507.